Breaking the field-of-view limit in augmented reality with a scanning waveguide display

JIANGHAO XIONG, GUANJUN TAN, TAO ZHAN, ![ID] AND SHIN-TSON WU* ![ID]

College of Optics and Photonics, University of Central Florida, Orlando, FL 32816, USA
*swu@creol.ucf.edu

Abstract: The ultimate augmented reality (AR) should be a glass-type see-through display with uncompromised optical performances. The major technical challenge of present AR display systems is to fulfill wide field-of-view (FOV) and large eye box simultaneously for a comfortable visual experience. Here, we propose a novel scanning waveguide display to break the theoretical limit of present waveguide displays while maintaining a large eye box. The core component is an off-axis reflective lens array, which is fabricated by an innovative chiral liquid crystal polarization holography method. The lens array consists of 8×15 lenslets whose pitch length is 2 mm and f-number is 0.41 at 639 nm. Such a scanning waveguide display dramatically extends the diagonal FOV from the state-of-the-art 52° (HoloLens 2) to 100°. These approaches not only significantly advance the optical design of present AR display systems but also open new applications to a broad range of optical systems, including high-precision imaging, sensing, and advanced photonic devices.

1. Introduction

Augmented reality (AR) provides ubiquitous experience by superimposing digital content with real world and is emerging as next-generation display technology with widespread applications in education, healthcare, engineering, and entertainment, to name a few [1,2]. The goal of an AR display is to have a glasses-type form factor with excellent image quality for comfortable daily wear. To this end, several schemes have been introduced, including reflection-type [3–6], retinal scanning [7–10] and waveguide display [11–15]. Unfortunately, unlike Moore's law in electronics that enables squeezing the size of electronic components while improving the performance, shrinking the dimension of optical systems ultimately encounters the limit of étendue conservation [16]. For a conventional system like reflection-type AR with fixed étendue, the product of eye box size and field-of-view (FOV) is conserved. Further improving the performance will inevitably demand a larger optics.

To overcome the étendue conservation, novel display mechanisms such as retinal scanning [7–10] and waveguide display [11–15] have been proposed. The retinal scanning method uses an off-axis lens coupler to form a Maxwellian view directly on the viewer's retina, as outlined in Fig. 1(a). Its FOV is directly determined by the f-number ($f/\#$) of the coupler lens and therefore is not bounded, but it suffers from the tiny eye box of a single Maxwellian view. To enlarge the eye box requires multiplication [8] or steering [9] of the viewing points. On the other hand, waveguide display overcomes the étendue conservation through duplication of exit pupil by total internal reflection (TIR) of the propagating light. Thus, it provides a large eye box without sacrificing FOV, as Fig. 1(b) shows. However, in conventional waveguide displays, the light propagating angle is constrained by the lower limit of TIR condition and the upper limit to maintain good uniformity of out-coupled light, which sets a theoretical limit of total FOV. This limitation is largely due to the employed out-coupler, which is usually a grating with fixed deflection angle but without any optical power. Hence, the angle of out-coupled light is only related to the propagating angle of TIR. To break this correlation, we propose to replace the
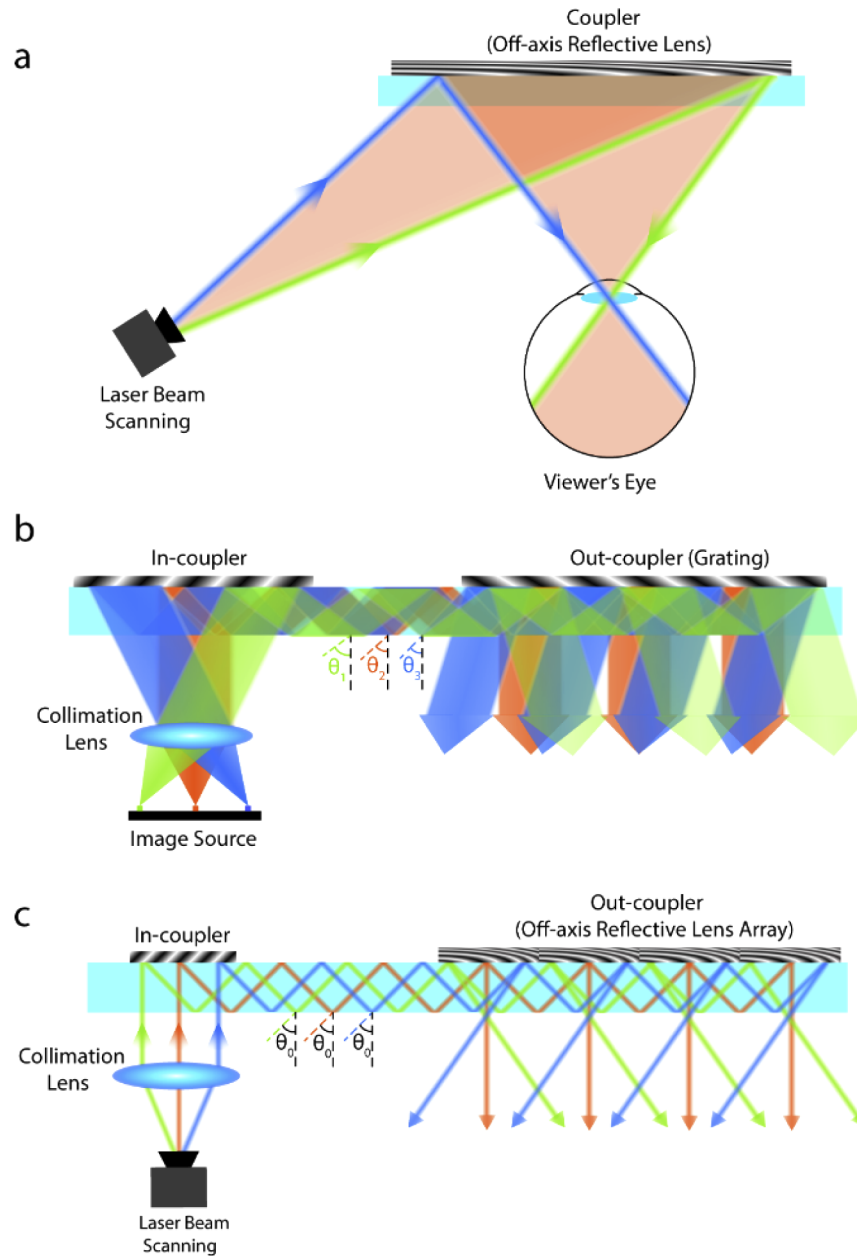
Fig. 1. Schematic diagram of different see-through display systems: (a) Retinal scanning display with a scanning laser beam and an off-axis combiner lens. (b) Traditional waveguide display with light paths of three pixels. The propagation angle in the waveguide is different for each pixel. (c) Our proposed scanning waveguide display with illustration of light paths of three pixels. The propagation angle in the waveguide is fixed for all pixels.

grating by a lens-array component, which offers high optical power and eyebox expansion at the same time. This way, the burden of producing light with different angles can be shifted from TIR process to the lens-array component. Such an AR display combines the wide FOV of retinal scanning and the large eye box of waveguide display. Therefore, we call it scanning waveguide display (SWD). As Fig. 1(c) depicts, the propagation angle in the SWD is fixed for all the incident light rays. Separation of different pixels is achieved by controlling the relative shift of the rays to reach different portion of the out-coupler lens, therefore obtaining different diffraction angles.

To fulfill the new design challenge of our proposed SWD, we demonstrate a new method for fabricating an off-axis reflective chiral lens array with $f/\# = 0.41$ using chiral liquid crystal (CLC) polarization holography. In addition, through the analysis of polarization holography we find this method is versatile for fabricating a broad range of optical components. By adopting the chiral lens array, we construct a SWD with a diagonal FOV of 100°, which exceeds the theoretical limit (~78°) of a conventional waveguide display. Our proposed system not only breaks the FOV limit in conventional waveguide displays but also enables a new round of developments in imaging and display devices due to the fabrication versatilities of the novel CLC polarization holography.

2. Results

2.1. Design of scanning waveguide display

A traditional waveguide display relies on different propagating angles of light in the waveguide to achieve separation of pixels. As Fig. 1(b) depicts, the beams emitting from different pixels, after collimation, are coupled into the waveguide with different propagating angles θ_1 and θ_2. As the light propagates in the waveguide and encounters the out-coupler, a portion of the light gets coupled out while the remaining part keeps propagating and repeating the process. Because the out-coupler consists of a grating with uniform k-vector, the angle of each out-coupled light is the same and determined by the propagating angle in the waveguide. The lower limit of the propagating angle is the TIR critical angle determined by the refractive index of waveguide. The upper limit, on the other hand, usually comes from the engineering consideration that a too large angle will result in a large gap between two consecutive TIRs and decrease the uniformity of out-coupled light. The FOV with lower limit of TIR critical angle can be derived as (see Supplement 1)

$$FOV = 2\sin^{-1}\left[\frac{1}{2}(n_s \sin \theta_m - 1)\right], \qquad (1)$$

where n_s is the refractive index of the waveguide substrate and θ_m is the maximum propagating angle. Let us take $n_s = 2$ and $\theta_m = 90°$ as two extreme cases, then the theoretical limit of FOV is calculated to be 60° for one dimension, and 78° for the diagonal.

In our SWD system, as plotted in Fig. 1(c), the laser beams are collimated before entering the waveguide. Therefore, the propagating rays have a fixed propagating angle θ_0, but different position shift. To ensure that each single ray always hits the same position of each lenslet, we should have

$$p = 2h \tan \theta_0, \qquad (2)$$

where p is the pitch of the lenslet and h is the waveguide thickness. However, in the design of such a near-eye display system, the factor of human eye should also be considered. The separation of two rays produced by two consecutive out-couplings is the same as p, which should be smaller than the human eye pupil (2mm ~ 4mm) to ensure at least one ray entering the pupil at all time. Therefore, the pitch of each lenslet should not exceed 2mm.

Similar to the retinal scanning type, the FOV of SWD is solely determined by the $f/\#$ of the off-axis lens coupler. To obtain a FOV exceeding the theoretical limit of waveguide displays, say 80°, a $f/\# = 0.6$ is required. At the same time, to obtain comfortable viewing experience with, for example an eye box of 16mm by 16mm, an 8 by 8 array is required if the lenslet pitch is 2mm.

## 2.2. Chiral liquid crystal polarization holography

The fabrication of such an off-axis reflective lens array is quite challenging, which mainly originates from the off-axis and reflective features as well as the low *f/#* that entails large variation of light modulation power. The reason that the off-axis feature is required is because the propagating light in the waveguide has to be coupled out to distribute symmetrically around the normal direction, while the reflective attribute is necessary to avoid the diffraction of environmental light into undesired stray light. The off-axis reflective lens, similar to the coupler in Fig. 1(a), has a small diffraction angle on one edge (green arrow) and large angle on the other edge (blue arrow). As a result, the local grating period should be in the sub-wavelength to micron range.

Optical metasurfaces [17–21] have recently attracted considerable attentions due to their design flexibility to achieve numerous novel optical functions desired for imaging and display systems [19–21]. Current methods are mainly based on localized resonance, effective index and Pancharatnam-Berry phase [17,18], among which the localized resonance method is most suitable for fabricating off-axis reflective lenses because of its ability to control the reflection amplitude and phase. However, the deflection angle of such components is usually limited due to the coupling of neighboring resonators, especially when operating in the visible spectral region. The higher order diffractions could also become a problem for the see-through ability of the display. Another common issue of metasurfaces is that the typical size of the component is limited due to the high cost and low yield of e-beam lithography.

Therefore, we propose to use the self-assembled chiral liquid crystal together with polarization holography technique. The basic principle is to form linear polarization pattern through the interference of left-handed circularly polarized (LCP) light and right-handed circularly polarized (RCP) light, as plotted in Fig. 2(a). After exposure, the pattern is recorded onto the photo-alignment layer, which in turn replicates the alignment pattern to the LC directors. Normally, nematic liquid crystal (NLC) is placed on top of the photo-alignment layer to form the Pancharatnam-Berry phase optical elements [22–27] and the on-axis transmission lens array have been reported [22,23,25]. However, as the pattern period gets smaller, the LC alignment becomes more challenging. In order to maintain the LC directors in a planar structure that follows the alignment pattern, the pattern period has to be larger than the NLC layer thickness [28], which is usually fixed to satisfy half-wave retardation.

Reflective Pancharatnam-Berry optical elements (PBOE) have also been demonstrated [23,29,30] by replacing NLC with an CLC, which is NLC doped with chiral compound for forming self-assembled chiral structures, as indicated in Fig. 2(b). Such a PBOE usually has a large period in the horizontal direction (parallel to the substrate) in order to maintain the planar alignment of CLC and produce the reflective Berry-phase [30]. Therefore, the off-axis reflective lens reported in [29] has a small diffraction angle of 0.5°. It was later discovered that in the case of small horizontal period, CLC self-assembles the tilted helical structure that is compatible with small-period alignment pattern, as shown in Fig. 2(b). Instead of deforming the helical structure, the sinusoidal alignment pattern only gives the volume CLC a tilt angle to match the bottom k-vector. The overall free energy can still maintain a minimal value due to the well-preserved helical structure [31]. Previous works have demonstrated the fabrication of gratings using this technique [31–33], where the LCP and RCP beams are in the same plane of incidence and have equal incident angles on the sample to ensure linear polarization pattern. However, to fabricate a PB lens, we need to insert a low *f/#* lens to one arm, which introduces a large degree of asymmetry to the system.

Previous works have analyzed the influence of incident light on the recording process in polarization holography [34–36], but these studies are restricted to either symmetric incidence or small incident angle. To generalize the CLC polarization holography for fabricating a broader range of optical components, it is necessary to analyze the influence of asymmetric configurations
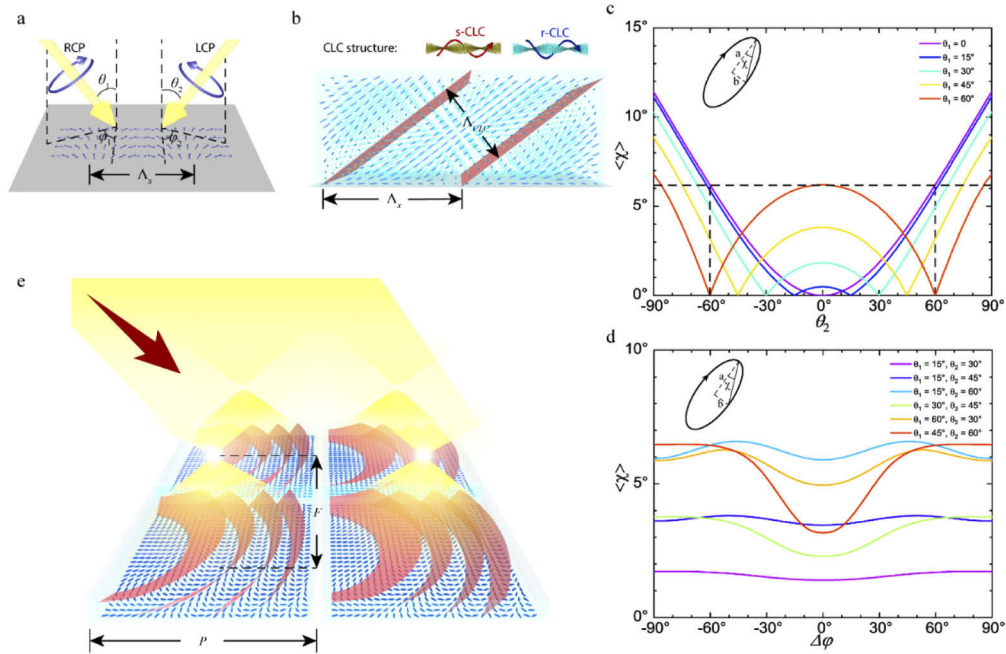
Fig. 2. Working principle of the CLC polarization holography. (a) The interference of RCP and LCP beams generating sinusoidal linearly polarized pattern. (b) (Upper) CLC helical structures with different handedness. (Lower) CLC molecular self-assembly forming tilted spiral structure that manifests the lowest free energy and matches the bottom alignment pattern. (c) Calculated relation between average ellipticity and beam incident polar angles, with zero azimuthal angle difference. (d) Calculated relation between average ellipticity and azimuthal angle difference. (e) Illustration of the off-axis reflective lens array, with the red surfaces indicating the Bragg surfaces of LC molecules. The volume distribution between adjacent Bragg surfaces resembles that in Fig. 2(b).

and large incident angles on the quality of linear polarization pattern. To this end, we define the average ellipticity as

$$\langle \chi \rangle = \left\langle \tan^{-1}(b/a) \right\rangle, \tag{3}$$

where a and b represent the length of long and short axes of the elliptical polarization (see Supplement 1). Let us discuss the first case when the incident polar angle θ_1 is fixed. Figure 2(c) shows the calculated results between ellipticity and polar angle θ_2. The second case is that both polar angles (θ_1 and θ_2) are fixed. Under such conditions, we need to know the relation between $\langle \chi \rangle$ and the difference of azimuthal angles ($\Delta\varphi = \varphi_1 - \varphi_2$). From Fig. 2(d), we find a large tolerance of the pattern linearity to the incident angle change. In our experiment, the incident angle of RCP light is 45°, while the LCP light has spatially variant polar angle from −34° to 34°. From Fig. 2(c), the worst scenario occurs at $\theta_1 = 45°$ and $\theta_2 = 0°$, with ellipticity of about 4°. More generally, when θ_1 and θ_2 are in the range from −60° to 60° and all possible azimuthal angles, the maximum ellipticity is about 6°, which would cause ~10% reduction to the interaction potential energy [37]. Therefore, the influence of the beam asymmetry on the photo-alignment relaxation time is negligible from device fabrication viewpoint.

When the linear polarization profile of the off-axis lens array is recorded onto the photo-alignment layer and a CLC layer is placed atop, which is similar to a grating, the CLC will locally form a tilted helical structure depicted in Fig. 2(b). But due to the spatial change of the pattern period and orientation, the tilted CLC structure will follow the change and form the spatially

varying local Bragg surface that focuses the oblique incident light onto the corresponding focal point, as plotted in Fig. 2(e).

2.3. Characterization of the CLC lens array

Figure 3(a) shows a photo of the fabricated chiral lens array with 8 by 15 lenslets. The dimension of each lenslet is 2mm by 2mm, and its reflective focal length is 1.15mm at 45° oblique incidence angle for a red light. The minified image (bright spots in the array) of two rectangular ceiling lamps above the sample is formed by each lenslet and reflected into the camera. On the other hand, the light from the background image is not influenced and it directly passes through the sample to the camera, which demonstrates an excellent see-through capability required by the AR system. The images of the lens array under polarizing optical microscope (POM) are shown in Figs. 3(b)–3(e). The fringe pattern is marked by the black dashed lines in Fig. 3(b). The largest fringe period is ~1.25μm as shown at the right edge of Fig. 3(c) and the smallest is ~0.38μm as depicted at the left corner of Fig. 3(e). The direction of the fringe pattern is also spatially variant to form the asymmetric parabolic shape that manifests off-axis focusing, therefore forming the pattern transition in Figs. 3(d) and 3(e).
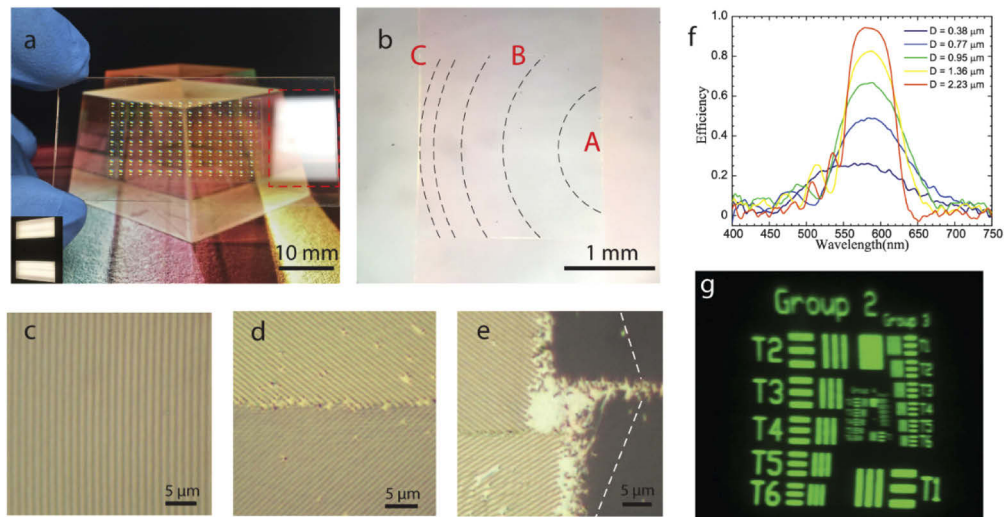

Fig. 3. Characteristics of the off-axis chiral lens array. (a) Full picture of the 8 by 15 lens array. The left bottom shows the image of two ceiling lamps. The box in red dashed line indicates the surface-reflected image of the lamp. (b) POM image of a single lenslet, with black dashed lines indicating the spatial variant fringe pattern. (c) Magnified POM image of region A in Fig. 3(b). (d) Magnified POM image of region B in Fig. 3(b). (e) Magnified POM image of region C in Fig. 3(b), where white dashed lines indicate the fringe direction. (f) Efficiency spectrum with different sample thickness. (g) Image of the 1951 USAF resolution target at λ=546 nm.

Similar to a Bragg grating whose reflection efficiency depends on the thickness, the chiral lens array also exhibits thickness-dependent efficiency spectrum as Fig. 3(f) shows. The thinnest sample (D=0.38μm) shows a relatively low efficiency (~20%) across the 500nm ~ 650nm bandwidth. As the thickness increases to 2.23 μm, the peak efficiency surges to nearly 95%, while the bandwidth (FWHM) decreases to around 50nm. Because our lens array is intended to be used as an out-coupler, we select the one with low efficiency (D=0.38 μm) due to its relatively uniform light output instead of out-coupling all the light at once.

To test the imaging performance of the sample, we placed a 1951 USAF resolution target at the oblique angle and observed the reflected image with a microscope, as shown in Fig. 3(g). Due to the off-axis nature of the imaging system, the astigmatism greatly decreases the resolution of the image, leading to a different resolving ability of the horizontal and vertical lines. Nonetheless, in a laser beam scanning system the influence of aberration on resolution is relatively insignificant because the laser beam only covers a very small region (beam waist) of the sample at each time frame. Therefore, the aberration only causes distortion on the final laser spot pattern, which can be digitally corrected.

2.4.   Scanning waveguide display system

Next, we built a SWD system with the fabricated chiral lens array and examined its display performance. The schematic drawing of the setup is shown in Fig. 4(a). The light source is a laser beam scanning (LBS) pico-projector. Because of the different diffraction angles for different colors, we only used the red channel to avoid the ghost images from color breakup. Full color image is achievable with separate waveguide layers stacked together (Fig. S7 in Supplement 1). Laser beams from the projector were firstly collimated by a lens and coupled into the waveguide by a prism. The image was self-duplicated by the TIR process in x direction. In y direction, we digitally duplicated the image by displaying a vertical line of identical images. When the laser ray encounters a single lenslet, it gets partially coupled out of the waveguide and focused to a point, forming an elemental Maxwellian view, as Fig. 4(b) depicts.
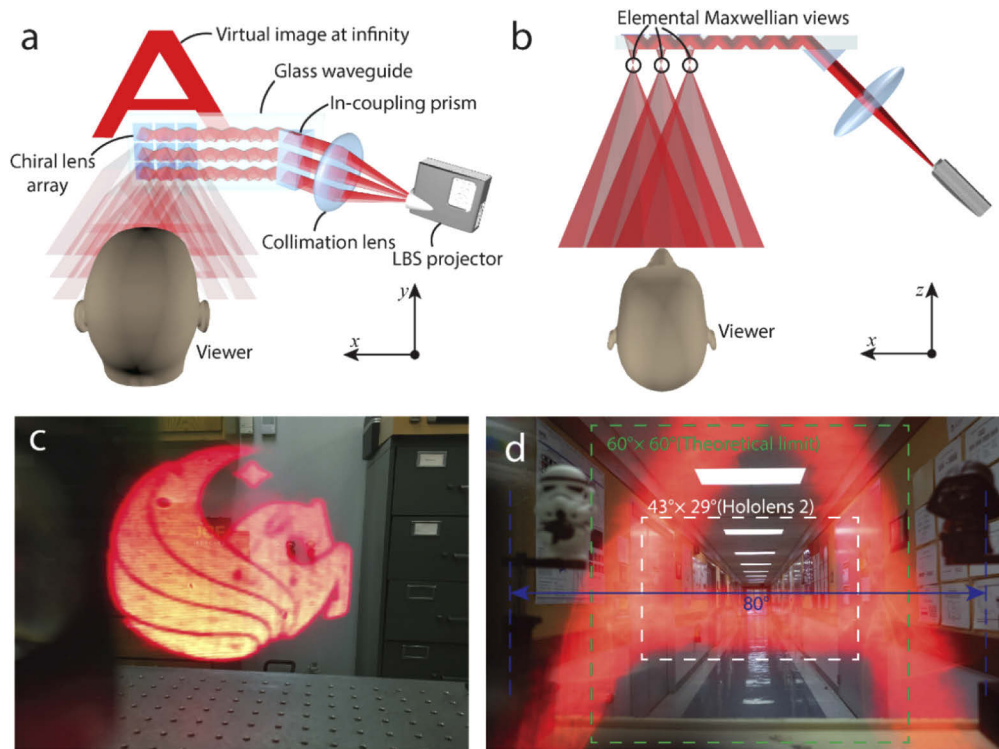
Fig. 4. Scanning waveguide display. (a) Schematic plot of the experimental setup. (b) Top view of the experimental setup demonstrating the formation of elemental Maxwellian views. (c) Captured image of the Maxwellian view from a single lenslet. (d) Captured picture of the full view from combined elemental images of each lenslet, with the FOV of 80° in horizontal (blue dashed line). Two objects (black and white) with separation 80° is placed for reference. The FOV of theoretical limit and Microsoft HoloLens 2 are shown in green and white dashed lines.

When the camera captures an elemental Maxwellian view and blocks the others with adjustment of the aperture location and size, the image will have the same appearance and property as the retinal scanning display, as shown in Fig. 4(c). However, this requires the camera aperture to be very close (∼ 1mm) to the waveguide. For the normal viewing experience of a glasses-type AR display, the distance from the viewer's eye pupil to the glasses is about 1 cm. In this case, the human eye (or camera) observes the overall image formed by stacking of elemental Maxwellian views, as shown in Fig. 4(d).

The lenslet size is closely related to the waveguide thickness. In experiment, we used a 1-mm-thick waveguide, which requires us to fabricate 2-mm by 2-mm lenslets. The lenslet size determines the spatial density of out-coupled rays. If the lenslet size is too small, the rays entering the eye pupil for each single pixel will increase. Because for each pixel the out-coupled rays are parallel, they will be focused to the same point on the retina when the eye is focused at infinity. However, a small lenslet size would decrease the resolution. On the other hand, if the lenslet size is too large, the 'dead zone' issue will manifest. This means some rays would not enter the eye pupil because the spatial gap between two consecutive out-coupled rays is larger than the pupil size. Therefore, in experiment we chose the lenslet size to be 2 mm, which is just below the lower limit of the eye pupil size.

As shown in Fig. 4(d), the horizontal FOV of the overall image is measured to be 80°. Due to the limitation from camera, the full vertical FOV cannot be captured. With the lenslet aspect ratio of 1:1, we conclude the diagonal FOV is 100°. In fabrication, the lenslets with $f/\# = 0.75$ (diagonal) are recorded by a blue laser (λ=457 nm). However, in the display system a red laser (λ=639 nm) is adopted so the actual $f/\#$ is reduced to 0.41, corresponding to a diagonal FOV of 102°, which is close to the measured experimental value. The FOV range well covers the theoretical limit of traditional waveguide displays (60°×60°), which is already sufficiently larger than that of current state-of-the-art product Microsoft Hololens 2 (43°×29°).

The eye box in our system is determined by both FOV and array size. It manifests a 3D shape plotted in Fig. S9 in Supplement 1, with dimension in z direction about 1 cm. The closer the eye moves to the out-coupler, the larger the area of intersection of 3D eye box is. For example, if the eye is positioned at 7 mm from the out-coupler, then the moving range in the x-y plane is 18.25 mm by 4.25 mm. In practice, the eye box can be enlarged without limit by adding more lenslets to the array.

Another common issue in waveguide displays is the uniformity of out-coupled light. The measured spatial deviation of light intensity in our system is about 4% (2.4 μW) of the total out-coupled light (54 μW), with total out-coupling efficiency about 40%. For angular uniformity, the deviation across the entire FOV is about 4.5%. In traditional waveguide displays, there usually exists a trade-off between FOV and uniformity because the large-angle light in waveguide results in a big spatial separation between consecutive out-couplings. But in SWD, there is no such concern because the propagating angle is fixed. Additionally, with proper management of the polarization state after each TIR (Fig. S10 in Supplement 1), both uniformity and efficiency have potential to reach 100% (see Supplement 1 for details).

3. Discussion

Although our new SWD exhibits a significantly wider FOV while keeping a large eye box, its resolution is compromised. We attribute this phenomenon to two factors. The first reason comes from the digital duplication that directly divides the projector resolution by 8. For actual application, the digital duplication can be replaced by a so-called fold grating [10] in a waveguide display to optically expand the image in the *y* direction without sacrificing the original resolution (Fig. S5 in Supplement 1). The second reason is related to the Gaussian beam profile. The resolution density (pixel per degree, or PPD) of the system is directly determined by the spot size of the Gaussian beam on viewer's retina. A resolution density of 40 PPD corresponds

to the spot size of 10 μm. In principle, we can set the Gaussian beam waist on the retina and back-trace the Gaussian beam to obtain the required profile in the waveguide. In our experiment, unfortunately, the degree of freedom for adjustment is limited because it is difficult to take apart the LBS and adjust the beam profile without damaging the laser module. Still, there exists a huge room for improvement by adopting the Gaussian beam confinement [38–42] or non-diffractive beam [43,44] (see Supplement 1). Alternatively, a functional contact lens [45] can be adopted to focus the display light onto the retina, which can achieve a resolution density of 80 PPD (see Supplement 1).

In conclusion, we propose and build a SWD that adopts both advantages of pupil expansion by TIR in waveguide display and wide FOV in retinal scanning display. The essential part of the system is an off-axis reflective lens array, which is fabricated by a novel CLC polarization holography method. The method is studied and confirmed to accommodate a wide range of CLC optical components, offering new applications in various optical systems. The SWD, on the other hand, breaks the limit of FOV and eye box size in see-through displays, providing a new concept and understanding of the display system. Further improvements in terms of image quality and depth generation are also possible with more design freedoms in laser beam profile and system-level pupil expansion.

4.   Materials and methods

4.1.   Fabrication

Our polarization holography system consisted of a two-arm interferometer (Fig. S3 in Supplement 1). The laser source (Cobolt Twist 457nm 200mW), after spatial filtering and expansion, was split into two beams by a non-polarizing beam splitter. In each beam path, a quarter-wave plate was used to control the polarization state to LCP and RCP, respectively. An aspheric lens with diameter of 10 mm and focal length of 7.5 mm (Edmund 69-856) was placed in the first arm to focus the light into a 2-mm by 2-mm square hole mask. The second beam was at 45° with respect to the first beam. Another long-focus lens ($f = 20$cm, Thorlabs AC508-200-A) was placed in the second arm to collect the light and equalize the intensity of two beams. The laser power was set at 100 mW and the light intensity behind the hold mask was measured to be 115 mW/cm^2.

The first step of the fabrication process was to clean the glass substrate with ethanol, acetone and isopropyl-alcohol. Then the photo-alignment material brilliant yellow (from Tokyo Chemical Industry, 0.2 wt.% in dimethyl-formamide) was spin-coated onto the substrate at 500 rpm ramp for 5s followed by 3000 rpm for 30s. After that, the sample was placed in the polarization holography system for exposure. The exposure time for each lenslet was 15s and a 2D translation stage was adopted to move the sample to repeat the exposure process. Then, a layer of reactive mesogen mixture (RMM) was spin-coated onto the sample. The precursor of RMM consisted of 2 wt.% R5011 (from HCCH), 3 wt.% photo-initiator Irgacure 651 (from BASF) and 95 wt.% RM257 (from LC Matter). The precursor was diluted in toluene to form the RMM solution for spin-coating. Finally, the sample was cured under UV light (356 nm) with a dosage of ~3 J/cm^2 (5min with ~10 mW/cm^2 power density). The detailed dilution ratios of RMM and spin-coating speeds for different sample thickness can be found in Supplement 1.

4.2.   Measurement

The efficiency of the sample is characterized using the setup depicted in Fig. S4 in Supplement 1. The transmission spectrum of the sample was measured with a collimated light from a halogen lamp and a spectrometer (Ocean Optics model HR4000CG-UV-NIR). The efficiency spectrum was calculated by subtracting one with the transmission spectrum, with the assumption that all other diffraction orders are negligible. The microscope for capturing the picture is Olympus BX51 with a CCD camera Infinity 2-2.

OSA CONTINUUM

4.3. Display system

The imaging source of the scanning waveguide system is a LBS pico-projector (Sony MP-CL1) with resolution of 1920 by 720. The wavelength of the red color is 639 nm. In experiment, another notch filter (Thorlabs FL635-10) was placed at the projector output to filter out the green and blue lights. The thickness of the glass waveguide is 1 mm. The chiral lens array has a size of 8 by 15, lens pitch of 2 mm and focal length of 1.5 mm at the recorded wavelength (457 nm) and 1.15 mm for display wavelength (639 nm). The collimation lens has a focal length of 20 mm. The propagating angle of the laser rays in waveguide was adjusted to be 45° to match the waveguide thickness and lens pitch. The camera for taking the picture is Sony Alpha a7II with camera lens Sony SEL16F28.

Disclosures

The authors declare no competing financial interests or conflicts of interest.

See Supplement 1 for supporting content.

References

1. D. Van Krevelen and R. Poelman, "A survey of augmented reality technologies, applications and limitations," Int. J. Virtual Reality **9**(2), 1–20 (2010).
2. J. Geng, "Three-dimensional display technologies," Adv. Opt. Photonics **5**(4), 456–535 (2013).
3. K. Akşit, W. Lopes, J. Kim, P. Shirley, and D. Luebke, "Near-eye varifocal augmented reality display using see-through screens," ACM Trans. Graph. **36**(6), 1–13 (2017).
4. G. Li, D. Lee, Y. Jeong, J. Cho, and B. Lee, "Holographic display for see-through augmented reality using mirror-lens holographic optical element," Opt. Lett. **41**(11), 2486–2489 (2016).
5. D. Cheng, Y. Wang, H. Hua, and J. Sasian, "Design of a wide-angle, lightweight head-mounted display using free-form optics tiling," Opt. Lett. **36**(11), 2098–2100 (2011).
6. H. Huang and H. Hua, "High-performance integral-imaging-based light field augmented reality display using freeform optics," Opt. Express **26**(13), 17578–17590 (2018).
7. G. Westheimer, "The maxwellian view," Vision Res. **6**(11-12), 669–682 (1966).
8. S.-B. Kim and J.-H. Park, "Optical see-through Maxwellian near-to-eye display with an enlarged eyebox," Opt. Lett. **43**(4), 767–770 (2018).
9. M. K. Hedili, B. Soner, E. Ulusoy, and H. Urey, "Light-efficient augmented reality display with steerable eyebox," Opt. Express **27**(9), 12572–12581 (2019).
10. J. Kim, Y. Jeong, M. Stengel, K. Akşit, R. Albert, B. Boudaoud, T. Greer, J. Kim, W. Lopes, Z. Majercik, P. Shirley, J. Spjut, M. McGuire, and D. Luebke, "Foveated AR: dynamically-foveated augmented reality display," ACM Trans. Graph. **38**(4), 1–15 (2019).
11. B. Kress, *Optical waveguide combiners for AR headsets: features and limitations*, SPIE Digital Optical Technologies (SPIE, 2019), Vol. 11062.
12. J. Waldern, A. Grant, and M. Popovich, *DigiLens switchable Bragg grating waveguide optics for augmented reality applications*, SPIE Photonics Europe (SPIE, 2018), Vol. 10676.
13. Z. Liu, Y. Pang, C. Pan, and Z. Huang, "Design of a uniform-illumination binocular waveguide display with diffraction gratings and freeform optics," Opt. Express **25**(24), 30720–30731 (2017).
14. Y. Weng, Y. Zhang, J. Cui, A. Liu, Z. Shen, X. Li, and B. Wang, "Liquid-crystal-based polarization volume grating applied for full-color waveguide displays," Opt. Lett. **43**(23), 5773–5776 (2018).
15. J. Han, J. Liu, X. Yao, and Y. Wang, "Portable waveguide display system with a large field of view by integrating freeform elements and volume holograms," Opt. Express **23**(3), 3534–3549 (2015).
16. H. Gross, F. Blechinger, and B. Achtner, *Handbook of optical systems* (Wiley Online Library, 2005), Vol. 1.

17. K. Seyedeh Mahsa, A. Ehsan, A. Amir, and F. Andrei, "A review of dielectric optical metasurfaces for wavefront control," Nanophotonics **7**(6), 1041–1068 (2018).

18. P. Genevet, F. Capasso, F. Aieta, M. Khorasaninejad, and R. Devlin, "Recent advances in planar optics: from plasmonic to dielectric metasurfaces," Optica **4**(1), 139–152 (2017).

19. I. Kim, G. Yoon, J. Jang, P. Genevet, K. T. Nam, and J. Rho, "Outfitting Next Generation Displays with Optical Metasurfaces," ACS Photonics **5**(10), 3876–3895 (2018).

20. Z.-B. Fan, H.-Y. Qiu, H.-L. Zhang, X.-N. Pang, L.-D. Zhou, L. Liu, H. Ren, Q.-H. Wang, and J.-W. Dong, "A broadband achromatic metalens array for integral imaging in the visible," Light: Sci. Appl. **8**(1), 67 (2019).

21. G.-Y. Lee, J.-Y. Hong, S. Hwang, S. Moon, H. Kang, S. Jeon, H. Kim, J.-H. Jeong, and B. Lee, "Metasurface eyepiece for augmented reality," Nat. Commun. **9**(1), 4562 (2018).

22. M. Jiang, H. Yu, X. Feng, Y. Guo, I. Chaganava, T. Turiv, O. D. Lavrentovich, and Q.-H. Wei, "Liquid Crystal Pancharatnam–Berry Micro-Optical Elements for Laser Beam Shaping," Adv. Opt. Mater. **6**(23), 1800961 (2018).

23. S. V. Serak, D. E. Roberts, J.-Y. Hwang, S. R. Nersisyan, N. V. Tabiryan, T. J. Bunning, D. M. Steeves, and B. R. Kimball, "Diffractive waveplate arrays [Invited]," J. Opt. Soc. Am. B **34**(5), B56–B63 (2017).

24. L. De Sio, D. E. Roberts, Z. Liao, S. Nersisyan, O. Uskova, L. Wickboldt, N. Tabiryan, D. M. Steeves, and B. R. Kimball, "Digital polarization holography advancing geometrical phase optics," Opt. Express **24**(16), 18297–18306 (2016).

25. J. Xiong, T. Zhan, and S.-T. Wu, "A versatile method for fabricating Pancharatnam-Berry micro-optical elements," Opt. Express **27**(20), 27831–27840 (2019).

26. N. V. Tabiryan, S. V. Serak, S. R. Nersisyan, D. E. Roberts, B. Y. Zeldovich, D. M. Steeves, and B. R. Kimball, "Broadband waveplate lenses," Opt. Express **24**(7), 7091–7102 (2016).

27. J. Kim, Y. Li, M. N. Miskiewicz, C. Oh, M. W. Kudenov, and M. J. Escuti, "Fabrication of ideal geometric-phase holograms with arbitrary wavefronts," Optica **2**(11), 958–964 (2015).

28. H. Sarkissian, B. Park, N. Tabirian, and B. Zeldovich, "Periodically Aligned Liquid Crystal: Potential Application for Projection Displays," Mol. Cryst. Liq. Cryst. **451**(1), 1–19 (2006).

29. J. Kobashi, H. Yoshida, and M. Ozaki, "Planar optics with patterned chiral liquid crystals," Nat. Photonics **10**(6), 389–392 (2016).

30. R. Barboza, U. Bortolozzo, M. G. Clerc, and S. Residori, "Berry Phase of Light under Bragg Reflection by Chiral Liquid-Crystal Media," Phys. Rev. Lett. **117**(5), 053903 (2016).

31. J. Xiong, R. Chen, and S.-T. Wu, "Device simulation of liquid crystal polarization gratings," Opt. Express **27**(13), 18102–18112 (2019).

32. R. Chen, Y.-H. Lee, T. Zhan, K. Yin, Z. An, and S.-T. Wu, "Multistimuli-Responsive Self-Organized Liquid Crystal Bragg Gratings," Adv. Opt. Mater. **7**(9), 1900101 (2019).

33. Y.-H. Lee, K. Yin, and S.-T. Wu, "Reflective polarization volume gratings for high efficiency waveguide-coupling augmented reality displays," Opt. Express **25**(22), 27008–27014 (2017).

34. T. Huang and K. H. Wagner, "Holographic diffraction in photoanisotropic organic materials," J. Opt. Soc. Am. A **10**(2), 306–315 (1993).

35. M. Xu, D. K. G. D. Boer, C. M. V. Heesch, A. J. H. Wachters, and H. P. Urbach, "Photoanisotropic polarization gratings beyond the small recording angle regime," Opt. Express **18**(7), 6703–6721 (2010).

36. B. Kilosanidze and G. Kakauridze, "Polarization-holographic gratings for analysis of light. 1. Analysis of completely polarized light," Appl. Opt. **46**(7), 1040–1049 (2007).

37. V. G. Chigrinov, V. M. Kozenkov, and H.-S. Kwok, *Photoalignment of liquid crystalline materials: physics and applications* (John Wiley & Sons, 2008), Vol. 17.

38. A. S. Reyna and C. B. de Araújo, "Guiding and confinement of light induced by optical vortex solitons in a cubic–quintic medium," Opt. Lett. **41**(1), 191–194 (2016).

39. M. Peccianti, A. Dyadyusha, M. Kaczmarek, and G. Assanto, "Tunable refraction and reflection of self-confined light beams," Nat. Phys. **2**(11), 737–742 (2006).

40. A. Alberucci, C. P. Jisha, L. Marrucci, and G. Assanto, "Electromagnetic Confinement via Spin–Orbit Interaction in Anisotropic Dielectrics," ACS Photonics **3**(12), 2249–2254 (2016).

41. C. P. Jisha, A. Alberucci, J. Beeckman, and S. Nolte, "Self-Trapping of Light Using the Pancharatnam-Berry Phase," Phys. Rev. X **9**(2), 021051 (2019).

42. S. Slussarenko, A. Alberucci, C. P. Jisha, B. Piccirillo, E. Santamato, G. Assanto, and L. Marrucci, "Guiding light via geometric phases," Nat. Photonics **10**(9), 571–575 (2016).

43. W. T. Chen, M. Khorasaninejad, A. Y. Zhu, J. Oh, R. C. Devlin, A. Zaidi, and F. Capasso, "Generation of wavelength-independent subwavelength Bessel beams using metasurfaces," Light: Sci. Appl. **6**(5), e16259 (2017).

44. F. O. Fahrbach, P. Simon, and A. Rohrbach, "Microscopy with self-reconstructing beams," Nat. Photonics **4**(11), 780–785 (2010).

45. M. Guillaumée, S. P. Vahdati, E. Tremblay, A. Mader, G. Bernasconi, V. J. Cadarso, J. Grossenbacher, J. Brugger, R. Sprague, and C. Moser, "Curved Holographic Combiner for Color Head Worn Display," J. Display Technol. **10**(6), 444–449 (2014).